

COMPUTING VOLUME BOUNDS OF INCLUSIONS BY EIT MEASUREMENTS*

GIOVANNI ALESSANDRINI^Δ, ANTONIO BILOTTA[◦], ANTONINO MORASSI[∇],
EDI ROSSET^Δ AND EMILIO TURCO*

ABSTRACT. The size estimates approach for Electrical Impedance Tomography (EIT) allows for estimating the size (area or volume) of an unknown inclusion in an electrical conductor by means of one pair of boundary measurements of voltage and current. In this paper we show by numerical simulations how to obtain such bounds for practical application of the method. The computations are carried out both in a 2-D and a 3-D setting.

1. INTRODUCTION

EIT is aimed at imaging the internal conductivity of a body from current and voltage measurements taken at the boundary. It is well known, [1], [2], that, even in the ideal situation in which all possible boundary measurements are available, the correspondence *boundary data* \rightarrow *conductivity* is highly (exponentially) unstable. As a consequence it is evident that, in practice, it is impossible to distinguish high resolution features of the interior from limited and noisy boundary data, [3].

Motivated by applications, a line of investigation pursued by many authors, [4], [5], [6], [7], [8], [9], [10], [11], has been the one of limiting the analysis to cases in which one seeks an unknown interior inclusion embedded in an otherwise known (may be even homogeneous) conductor, and whose conductivity is assumed to differ from the background.

Even in this restricted case, and even when full boundary data are available, the instability remains of exponential type [12].

It is therefore reasonable to further restrict the goal and attempt to evaluate some parameters expressing the size (area, volume) of the inclusion, disregarding its precise location and shape, having at our disposal one pair of boundary measurements of voltage and current. This approach, which can be traced back to [4], has been well developed theoretically, [13], [14], [15], [16], see also [17] and [18] for the analogous treatment in the linear elasticity framework. In order to describe such type of results we need first to introduce some notation.

We denote by Ω a bounded domain in \mathbb{R}^n , $n = 2, 3$, representing an electrical conductor. The boundary $\partial\Omega$ of Ω is assumed of Lipschitz class, with constants r_0 , M_0 , that is the boundary can be locally represented as a graph of a Lipschitz continuous function with Lipschitz constant M_0 in some ball of radius r_0 . When no inclusion is present in the conductor we assume that it is homogeneous and we pose

Date: December 22, 2006.

2000 Mathematics Subject Classification. 35R30, 35R25, 73C02.

Key words and phrases. Size estimates, electrical impedance tomography.

*Work supported by MIUR, PRIN no. 2004011204.

its conductivity $\sigma(x) \equiv 1$. When the conductor contains an unknown inclusion D of different conductivity, say $k > 0$, $k \neq 1$ the overall conductivity in the conductor will be given by $\sigma(x) = 1 + (k - 1)\chi_D(x)$. Here and in what follows it is assumed that D is strictly contained in Ω . More precisely, for a given $d_0 > 0$,

$$\text{dist}(D, \partial\Omega) \geq d_0. \quad (1.1)$$

Let $\varphi \in H^{-\frac{1}{2}}(\partial\Omega)$, $\int_{\partial\Omega} \varphi = 0$, be an applied current density on $\partial\Omega$. The induced electrostatic potential $u \in H^1(\Omega)$ is the solution of the Neumann problem

$$\begin{cases} \text{div}((1 + (k - 1)\chi_D)\nabla u) = 0, & \text{in } \Omega, \\ \nabla u \cdot \nu = \varphi, & \text{on } \partial\Omega, \end{cases} \quad (1.2)$$

where ν denotes the outer unit normal to $\partial\Omega$.

When D is the empty set, that is when the inclusion is absent, the reference electrostatic potential $u_0 \in H^1(\Omega)$ satisfies the Neumann problem

$$\begin{cases} \Delta u_0 = 0, & \text{in } \Omega, \\ \nabla u_0 \cdot \nu = \varphi, & \text{on } \partial\Omega. \end{cases} \quad (1.3)$$

In both cases (1.2) and (1.3), the solutions u and u_0 are determined up to an additive constant.

Let us denote by W , W_0 the powers required to maintain the current density φ on $\partial\Omega$ when D is present or it is absent, respectively. Namely

$$W = \int_{\partial\Omega} u \varphi = \int_{\Omega} (1 + (k - 1)\chi_D) |\nabla u|^2, \quad (1.4)$$

$$W_0 = \int_{\partial\Omega} u_0 \varphi = \int_{\Omega} |\nabla u_0|^2. \quad (1.5)$$

The size estimate approach developed in [13], [14], [15], [16], tells us that the measure $|D|$ of D can be bounded from above and below in terms of the quantity $\left| \frac{W_0 - W}{W_0} \right|$ which we call the normalized power gap. More precisely the following bounds hold, see [16, Theorem 2.3].

Theorem 1.1. *Let D be any measurable subset of Ω satisfying (1.1). Under the above assumptions, if $k > 1$ we have*

$$\frac{1}{k-1} C_1^+ \frac{W_0 - W}{W_0} \leq |D| \leq \left(\frac{k}{k-1} \right)^{\frac{1}{p}} C_2^+ \left(\frac{W_0 - W}{W_0} \right)^{\frac{1}{p}}. \quad (1.6)$$

If, conversely, $k < 1$, then we have

$$\frac{k}{1-k} C_1^- \frac{W - W_0}{W_0} \leq |D| \leq \left(\frac{1}{1-k} \right)^{\frac{1}{p}} C_2^- \left(\frac{W - W_0}{W_0} \right)^{\frac{1}{p}}, \quad (1.7)$$

where C_1^+ , C_1^- only depend on d_0 , $|\Omega|$, r_0 , M_0 , whereas $p > 1$, C_2^+ , C_2^- only depend on the same quantities and, in addition, on the frequency of φ

$$F[\varphi] = \frac{\|\varphi\|_{H^{-\frac{1}{2}}(\partial\Omega)}}{\|\varphi\|_{H^{-1}(\partial\Omega)}}. \quad (1.8)$$

When it is a priori known that the inclusion D is not too small (if it is at all present), a situation which often occurs in practical applications, stronger bounds apply.

Theorem 1.2. *Under the above hypotheses, let us assume, in addition, that*

$$|D| \geq m_0, \quad (1.9)$$

for a given positive constant m_0 . If $k > 1$ we have

$$\frac{1}{k-1} C_1^+ \frac{W_0 - W}{W_0} \leq |D| \leq \frac{k}{k-1} C_2^+ \frac{W_0 - W}{W_0}. \quad (1.10)$$

If, conversely, $k < 1$, then we have

$$\frac{k}{1-k} C_1^- \frac{W - W_0}{W_0} \leq |D| \leq \frac{1}{1-k} C_2^- \frac{W - W_0}{W_0}, \quad (1.11)$$

where C_1^+ , C_1^- only depend on d_0 , $|\Omega|$, r_0 , M_0 , whereas C_2^+ , C_2^- only depend on the same quantities and, in addition, on m_0 and $F[\varphi]$.

Theorem 1.2 can be easily deduced from Theorem 1.1 by the arguments sketched in [19, Appendix].

One of the goals of the present paper is to test the applicability of such bounds by numerical simulations with the following purposes:

i) provide practical evaluations of the constants C_1^\pm , C_2^\pm appearing in the above inequalities (1.6), (1.7), (1.10), (1.11);

ii) when, due to special geometric configurations, it is possible to compute theoretically such constants, compare such theoretical values with those obtained by simulations;

iii) show that such upper and lower bounds deteriorate as the frequency $F[\varphi]$ increases.

The other goal of this paper is to perform similar kinds of numerical simulations when the so-called *complete model* of EIT is adopted. We recall that this model is aimed at an accurate description of the boundary measurements suitable for medical applications, and was introduced in [20] and subsequently developed in [21] and [22]. In this model, the metal electrodes behave as perfect conductors and provide a low-resistance path for current. An electrochemical effect at the contact between the electrodes and the body results in a thin, highly resistive, layer. The impedance of this layer is characterized by a positive quantity z_l on each electrode e_l , $l = 1, \dots, L$, which is called *surface impedance*.

Denoting by I_l the current applied to each e_l , the resulting boundary condition on each electrode e_l becomes

$$u + z_l \nabla u \cdot \nu = U^l, \quad \text{on } e_l, \quad (1.12)$$

where the unknown constant U^l is the voltage which can be measured at the electrode e_l .

We assume, as before, that the reference conductor has conductivity $\sigma \equiv 1$ and that an unknown inclusion D of conductivity $\sigma \equiv k$, with $k > 0$ and $k \neq 1$, is strictly contained in Ω . Therefore, the electrostatic potential u inside the conductor is determined, up to an additive constant, as the solution to the following problem

$$\begin{cases} \operatorname{div}((1 + (k-1)\chi_D)\nabla u) = 0, & \text{in } \Omega, \\ u + z_l \nabla u \cdot \nu = U^l, & \text{on } e_l, \ 1 \leq l \leq L, \\ \nabla u \cdot \nu = 0, & \text{on } \partial\Omega \setminus \bigcup_{l=1}^L e_l, \\ \int_{e_l} \nabla u \cdot \nu = I_l, & 1 \leq l \leq L, \end{cases} \quad (1.13)$$

where the so-called current pattern $I = (I_1, \dots, I_L)$ is subject to the conservation of charge condition $\sum_{l=1}^L I_l = 0$, and the unknown constants U^l are the components of the so-called voltage pattern $U = (U^1, \dots, U^L)$.

When the inclusion is absent, the electrostatic potential u_0 induced by the same current pattern I is determined, up to an additive constant, as the solution of the following problem

$$\begin{cases} \Delta u_0 = 0, & \text{in } \Omega, \\ u_0 + z_l \nabla u_0 \cdot \nu = U_0^l, & \text{on } e_l, \ 1 \leq l \leq L, \\ \nabla u_0 \cdot \nu = 0, & \text{on } \partial\Omega \setminus \bigcup_{l=1}^L e_l, \\ \int_{e_l} \nabla u_0 \cdot \nu = I_l, & \ 1 \leq l \leq L, \end{cases} \quad (1.14)$$

where, as before, the U_0^l are unknown constants in the direct problem (1.14).

We shall assume that the sets e_1, \dots, e_L , representing the electrodes, are open, pairwise disjoint, connected subsets of $\partial\Omega$ and, in addition,

$$\text{dist}(e_l, e_k) \geq \delta_1 > 0 \quad \text{for every } l, k, \ l \neq k. \quad (1.15)$$

The surface impedance z_l on e_l , $l = 1, \dots, L$, is assumed to be real valued and to satisfy the following bounds

$$0 < m \leq z_l \leq M, \quad \text{for every } l = 1, \dots, L. \quad (1.16)$$

In this formulation, the powers W and W_0 become

$$W = \sum_{i=1}^L I_i U^i, \quad (1.17)$$

$$W_0 = \sum_{i=1}^L I_i U_0^i. \quad (1.18)$$

Size estimates like those of Theorems 1.1, 1.2 were obtained for the complete model in [23]. In particular we have

Theorem 1.3. *Let D be any measurable subset of Ω satisfying (1.1) and let W , W_0 be given by (1.17), (1.18). Then, inequalities (1.6), (1.7) hold for $k > 1$ and $k < 1$, respectively, where the constants C_1^+ , C_1^- only depend on d_0 , $|\Omega|$, r_0 , M_0 , and C_2^+ , C_2^- and $p > 1$ only depend on the same quantities and, in addition, on δ_1 , M and m .*

Also in this case, the size estimates of $|D|$ can be improved to the form (1.10), (1.11) when condition (1.9) is satisfied.

In Section 2 we consider the standard EIT setting. We start by describing the finite element setup used in our numerical simulations in Section 2.1. Next (as a warmup) we consider a two-dimensional model in Section 2.2.

In Section 2.3 we consider the three-dimensional case and we discuss all items i), ii), iii) introduced above. In particular we observe that, comparing the results as the frequency $F[\varphi]$ increases, we have quite rapidly a serious deterioration of the bounds. This poses a severe warning on the limitations that have to be taken into account in the choice of the boundary current profile φ .

Section 3 is devoted to simulations with the complete EIT model. In this case it is reasonable analyze the case when only two electrodes, one positive and one negative, are attached to the surface of the conductor. In this case, the frequency function is not available from the data since we are not prescribing the boundary

current $\nabla u \cdot \nu|_{\partial\Omega}$ but only the current pattern, which is a 2-electrode configuration, is just the pair $(1, -1)$. In place of the frequency function, the parameters that may influence the constants in the volume bounds are: the width of the electrodes and the distance between them. We perform various experiments to test such variability.

2. NUMERICAL SIMULATIONS FOR THE EIT MODEL

2.1. Numerical model. The numerical model is based on the discretization of the energy functional $J : H^1(\Omega, \mathbb{R}^n) \rightarrow \mathbb{R}$

$$J(u) = \frac{1}{2} \int_{\Omega} (1 + (k-1)\chi_D) \nabla u \cdot \nabla u - \int_{\partial\Omega} \varphi u, \quad (2.1)$$

associated to the variational formulation of problem (1.2). The energy functional (2.1) has been discretized by using the High Continuity (HC) technique already presented in [24] and [25] in the context of linear elasticity. Accordingly, for 2-D problems the electric potential on the e -th finite element can be represented as

$$u_e = \sum_{i,j=1}^3 \phi_i(\xi_1) \phi_j(\xi_2) u_{ij}, \quad (2.2)$$

whereas for the 3-D case it assumes the form

$$u_e = \sum_{i,j,l=1}^3 \phi_i(\xi_1) \phi_j(\xi_2) \phi_l(\xi_3) u_{ijl}, \quad (2.3)$$

where the coordinates ξ_r , $r = 1, \dots, n$, span the unitary element domain $[-\frac{1}{2}, \frac{1}{2}]^n$, $n = 2, 3$, and u_{ij} , u_{ijl} are the HC parameters involved in the field interpolation on the generic element. The shape functions $\phi_i(\xi_r)$ are defined as

$$\begin{cases} \phi_1(\xi_r) = \frac{1}{8} - \frac{1}{2}\xi_r + \frac{1}{2}\xi_r^2, \\ \phi_2(\xi_r) = \frac{3}{4} - \xi_r^2, \\ \phi_3(\xi_r) = \frac{1}{8} + \frac{1}{2}\xi_r + \frac{1}{2}\xi_r^2. \end{cases} \quad (2.4)$$

The 1-D case illustrated in Figure 1 shows the meaning of the HC parameters. They allow to define the slopes of the interpolated function at the end points of the element. On the same figure one can see also the positions of the HC nodes and the shape functions (2.4).

Figure 2 shows a typical structured mesh on a rectangular domain and the nodes used for the approximation of the potential field in the 2-D case. For elements with a side lying on the boundary, in order to easily impose the Neumann boundary conditions, special shape functions are used. In practice, the external HC nodes are translated onto the boundary $\partial\Omega$ and the related HC parameters have the meaning of function values (see again Figure 2). In this case the shape functions relative to a *left* boundary ($\xi_r = -\frac{1}{2}$) and a *right* boundary ($\xi_r = \frac{1}{2}$) of the finite

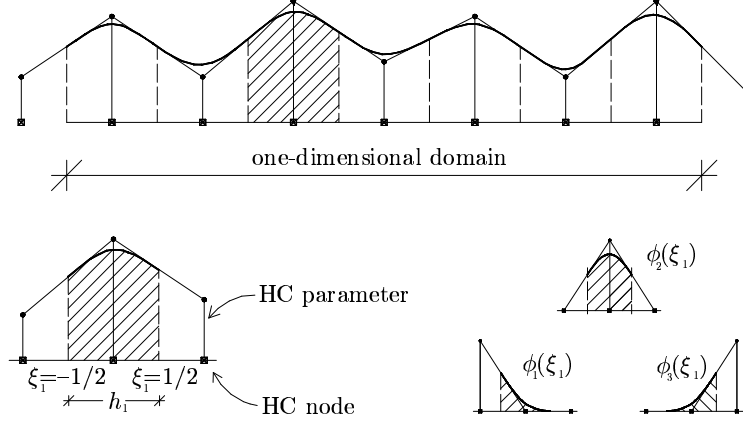


FIGURE 1. HC interpolation in the 1-D case: nodes, parameters and shape functions.

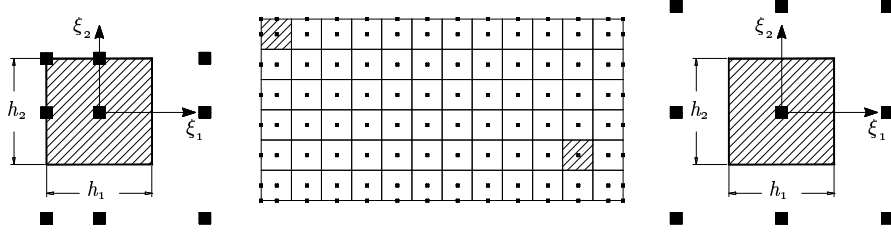


FIGURE 2. HC mesh in the 2-D case: nodes for boundary and inner elements.

element are

$$\text{left : } \begin{cases} \phi_1(\xi_r) = \frac{1}{4} - \xi_r + \xi_r^2, \\ \phi_2(\xi_r) = \frac{5}{8} + \frac{1}{2}\xi_r - \frac{3}{2}\xi_r^2, \\ \phi_3(\xi_r) = \frac{1}{8} + \frac{1}{2}\xi_r + \frac{1}{2}\xi_r^2; \end{cases} \quad \text{right : } \begin{cases} \phi_1(\xi_r) = \frac{1}{8} - \frac{1}{2}\xi_r + \frac{1}{2}\xi_r^2, \\ \phi_2(\xi_r) = \frac{5}{8} - \frac{1}{2}\xi_r - \frac{3}{2}\xi_r^2, \\ \phi_3(\xi_r) = \frac{1}{4} + \xi_r + \xi_r^2. \end{cases} \quad (2.5)$$

Further details about the HC interpolation can be found in [24] and [25]. This interpolation technique, which can be considered as a particular case of the Bézier interpolation, has the main advantage of reproducing potential fields of C^1 smoothness with a computational cost equivalent to a C^0 interpolation.

By (2.2) or (2.3), the potential field u on each element e takes the compact form

$$u_e = \mathbf{N}_e \mathbf{w}_e. \quad (2.6)$$

The one-row matrix \mathbf{N}_e collects the shape functions of the HC interpolation, whereas the components of the vector \mathbf{w}_e are the nodal parameters of the underlying element. With this notation, the gradient of the potential field is given by

$$\nabla u_e = \nabla \mathbf{N}_e \mathbf{w}_e. \quad (2.7)$$

We remark that the dimensions of the matrices \mathbf{N}_e , $\nabla \mathbf{N}_e$ and vector \mathbf{w}_e are 1×9 , 2×9 and 9×1 for the 2-D case and 1×27 , 3×27 and 27×1 for the 3-D case.

By (2.6) and (2.7), the discrete form of (2.1) becomes

$$J(\mathbf{w}_e) = \sum_e \left(\frac{1}{2} \int_{\Omega_e} (1 + (k-1)\chi_D) (\nabla \mathbf{N}_e \mathbf{w}_e) \cdot (\nabla \mathbf{N}_e \mathbf{w}_e) - \int_{\partial \Omega_e} \varphi \mathbf{N}_e \mathbf{w}_e \right), \quad (2.8)$$

or, in a compact form,

$$J(\mathbf{w}_e) = \sum_e (\mathbf{w}_e^T \mathbf{K}_e \mathbf{w}_e - \mathbf{w}_e^T \mathbf{p}_e). \quad (2.9)$$

The latter equation provides the definition of the matrix and vector associated to e -th element

$$\begin{cases} \mathbf{K}_e = \int_{\Omega_e} (1 + (k-1)\chi_D) (\nabla \mathbf{N}_e)^T \nabla \mathbf{N}_e, \\ \mathbf{p}_e = \int_{\partial \Omega_e} \varphi \mathbf{N}_e, \end{cases} \quad (2.10)$$

which can be used to assemble, by using standard techniques, the system of equations to solve.

2.2. Two-dimensional case. Numerical analysis has been performed on a square conductor Ω of side l under the two current density fields φ illustrated in Figure 3. The domain Ω has been discretized with a mesh of 21×21 HC finite elements and for both Test T_1 and Test T_2 of Figure 3 we have considered an inclusion D with conductivity $k = 0.1$ or $k = 10$.

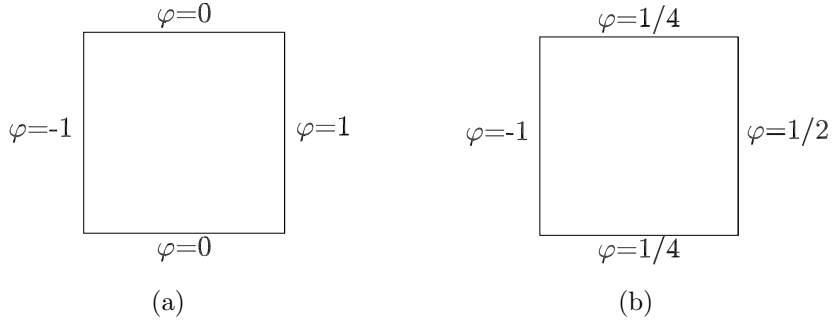


FIGURE 3. Square conductor considered in 2-D numerical simulations for the EIT model and applied current density fields: Test T_1 (a), Test T_2 (b).

A first series of experiments has been carried out by considering all possible square inclusions with side ranging from 1 to 5 elements, that is the size of inclusion has been kept lower than 6% of the total size of the conductor. The results are collected in Figures 4 and 5 for different values of the minimum distance d_0 between the inclusion D and the boundary of Ω .

From Figures 4(a) and 5(a), which refer to the case $k = 0.1$, one can note that the upper bound of $|D|$ is rather insensitive to the choice of d_0 , whereas the lower

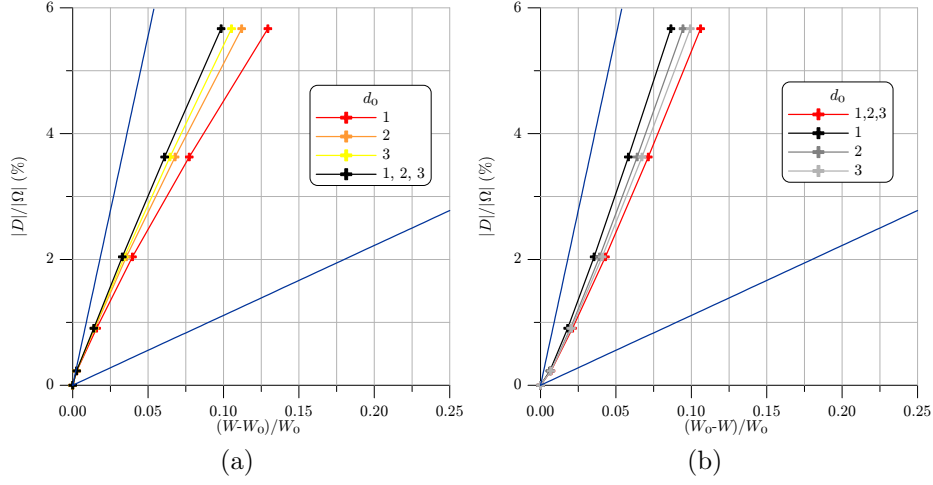


FIGURE 4. Influence of d_0 for square inclusions in Test T_1 of Figure 3(a) (21×21 FE mesh): $k = 0.1$ (a), $k = 10$ (b).

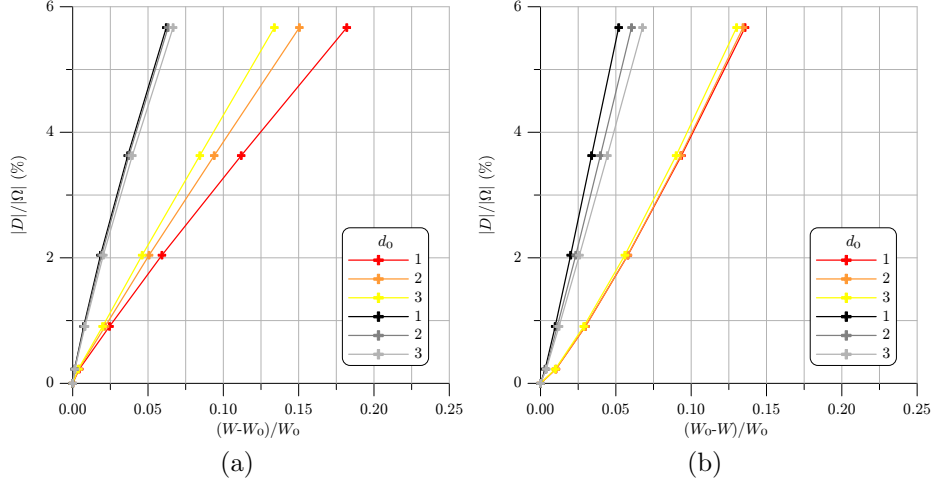


FIGURE 5. Influence of d_0 for square inclusions in Test T_2 of Figure 3(b) (21×21 FE mesh): $k = 0.1$ (a), $k = 10$ (b).

bound in (1.11) improves as d_0 increases. The converse situation occurs when the inclusion is made by material of higher conductivity, see Figures 4(b) and 5(b).

As a second class of experiments, we have considered inclusions of general shape on a FE mesh of 15×15 HC elements. More precisely, each inclusion is the union of elements having at least a common side and being at least $d_0 = 2$ elements far from the boundary $\partial\Omega$. Results are collected in Figures 6 and 7.

The straight lines drawn in Figures 4 and 6 correspond to the theoretical size estimates for test T_1 of Figure 3(a). For both cases $k = 0.1$ and $k = 10$ we have

$$\frac{1}{9} \frac{|W - W_0|}{W_0} \leq \frac{|D|}{|\Omega|} \leq \frac{10}{9} \frac{|W - W_0|}{W_0}. \quad (2.11)$$

The comparison with the region of the plane $\left(\frac{|D|}{|\Omega|}, \frac{|W-W_0|}{W_0}\right)$ covered by the corresponding numerical experiments confirms, as already remarked in [19] in the context of linear elasticity, that practical applications of the size estimates approach lead to less pessimistic results with respect to those obtained via the theoretical analysis.

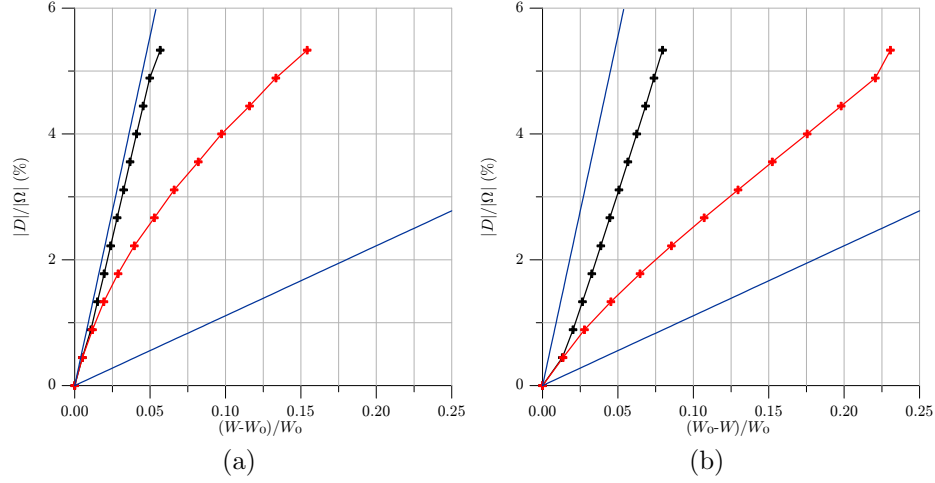


FIGURE 6. Numerical size estimates for inclusions of general shape generated from a generic element inside Ω for test T_1 of Figure 3(a) (21×21 FE mesh, $d_0 = 2$): $k = 0.1$ (a), $k = 10$ (b).

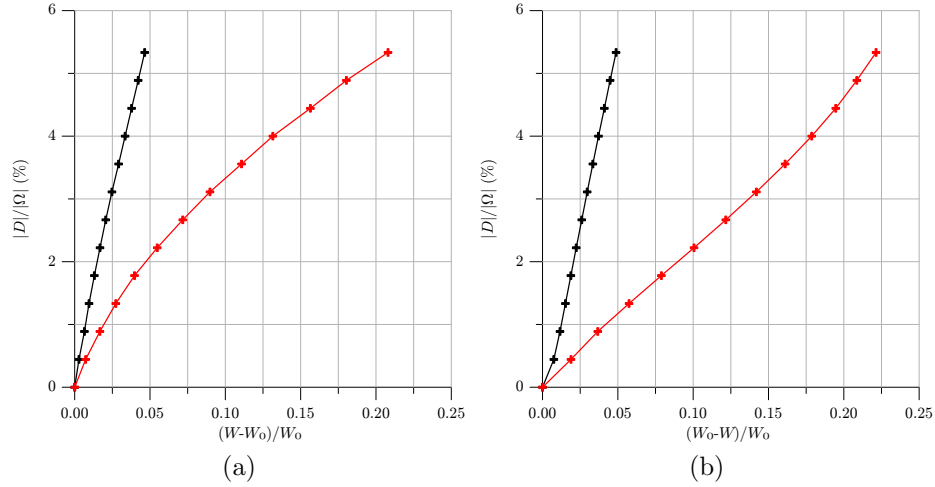


FIGURE 7. Numerical size estimates for inclusions of general shape generated from a generic element inside Ω for test T_2 of Figure 3(b) (21×21 FE mesh, $d_0 = 2$): $k = 0.1$ (a), $k = 10$ (b).

2.3. Three-dimensional case. The first part of this subsection is devoted to the extension to the 3-D case of the numerical simulations given in 2.2. In the second part, we shall investigate on the effect of the oscillation character of the Neumann data on the upper bound of size inclusion.

Similarly to the 2-D case, a first series of numerical simulations has been performed on an electrical conductor of cubic shape, of side l , with the two current density fields illustrated in Figure 8. In both cases, a mesh of $20 \times 20 \times 20$ finite elements has been considered when performing simulations in presence of cubic inclusions. The results are illustrated in Figures 9 and 10. Figure 9 contains also the straight lines corresponding to the theoretical size estimates for test T_1 of Figure 8, that is

$$\frac{1}{9} \frac{|W - W_0|}{W_0} \leq \frac{|D|}{|\Omega|} \leq \frac{10}{9} \frac{|W - W_0|}{W_0}. \quad (2.12)$$

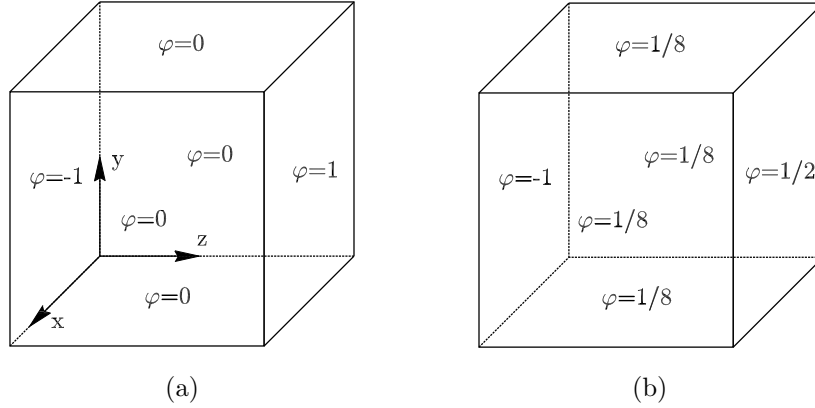


FIGURE 8. Cubic conductor considered in 3-D numerical simulations for the EIT model and applied current density fields: Test T_1 (a) and Test T_2 (b).

In order to deal with inclusions of general shape, however, the numerical experiments require some restrictions to reduce the computer time. A rough estimate of the computational cost can be obtained noting that the numerical effort is essentially due to the decomposition of the matrix associated to the linear system (2.9) and to the computation of its solution. Denoting by m the number of the equations and by b the half bandwidth of the matrix, the decomposition requires $m(b - 1)$ multiplications and $mb(b - 1)$ additions, whereas the computation of the solution involves mb multiplications.

Therefore, for each given inclusion in a $20 \times 20 \times 20$ FE mesh, a linear system of 10648 ($b = 1015$) equations has to be solved, requiring a computer time of approximately 86 s working on an Opteron 2.4 GHz computer. Since the number of all possible inclusions formed by n_i elements on a mesh of $n_e \times n_e \times n_e$ is $\frac{n_e^3!}{n_i!(n_e^3 - n_i)!}$, the way to calculate all the possible case is practically impossible. Indeed by considering that the $20 \times 20 \times 20$ is formed by 8000 elements and that, if the ratio $|D|/|\Omega|$ is less than 6% that is 480 elements, the number of cases to analyze is 69.1183×10^{785} .

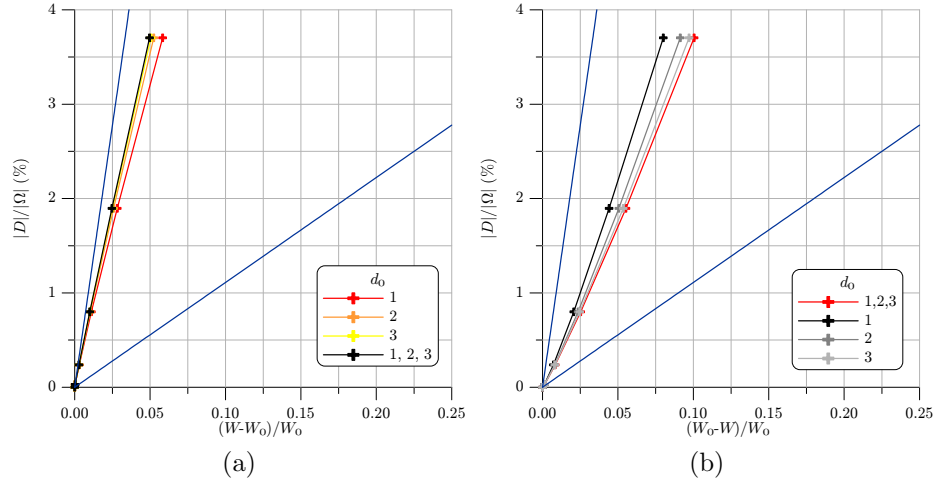


FIGURE 9. Influence of d_0 for cubic inclusions in test T_1 of Figure 8 ($20 \times 20 \times 20$ FE mesh): $k = 0.1$ (a), $k = 10$ (b).

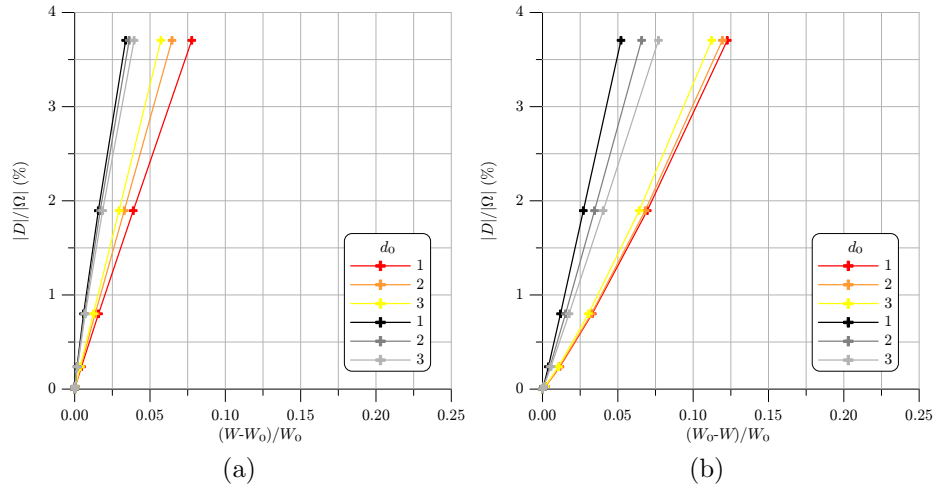


FIGURE 10. Influence of d_0 for cubic inclusions in test T_2 of Figure 8 ($20 \times 20 \times 20$ FE mesh): $k = 0.1$ (a), $k = 10$ (b).

In order to reduce the computer time significantly we have considered a $7 \times 7 \times 7$ mesh generating a system of 729 equations. Despite of this, the number of possible cases to consider still remains very high; for instance, for inclusions formed by 5 elements, one should solve about 3.8×10^{10} linear systems. Therefore, we decided to restrict our analysis to inclusions satisfying the following additional hypotheses:

- i) the inclusion is the union of elements having at least one common face and it is formed by starting from a generic element inside an octant of the cube (this last assumption is not really restrictive due to the symmetries of the problem);
- ii) $d_0 = 1$.

For inclusions formed by 1, ..., 7 elements, we have considered all possible inclusions satisfying the limitations *i*) and *ii*), whereas for inclusions formed by 8, ..., 17 elements we have considered a random sample because of the high computational cost. For these cases, the ratio between the sample dimension and that of all the data approximately spans between 20% for inclusions formed by 8 elements and 0.01% for inclusions formed by 17 elements. The results are presented in Figures 11 and 12 for Test T_1 and Test T_2 , respectively. In Figure 11, the straight lines corresponding to the theoretical bounds (2.12) for Test T_1 are also drawn. As already remarked in the treatment of the 2-D case, the theoretical analysis leads to rather pessimistic results with respect to those obtained by the numerical simulations, especially when the inclusion is softer than the surrounding material.

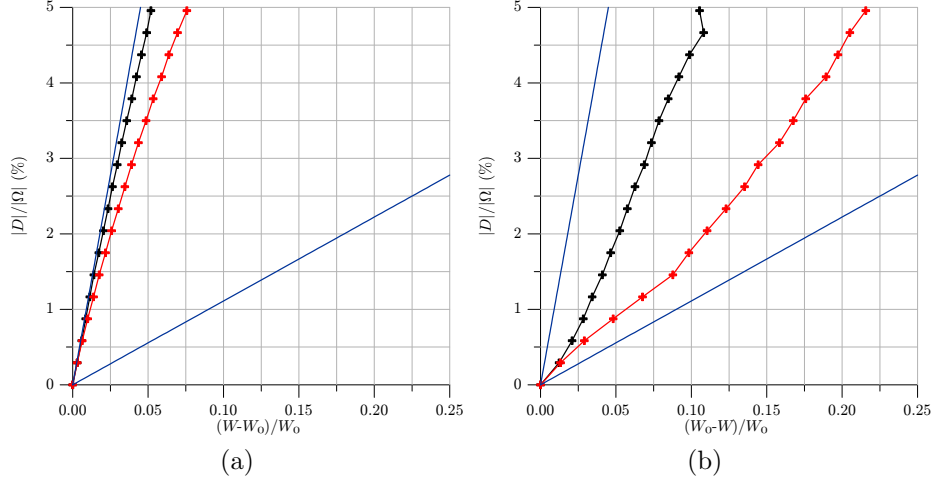


FIGURE 11. Numerical size estimates for inclusions of general shape generated from a generic element belonging to an eight of the cube for test T_1 of Figure 8(a) ($7 \times 7 \times 7$ FE mesh, $d_0 = 1$): $k = 0.1$ (a), $k = 10$ (b).

The Neumann data considered in the above experiments give raise to potential fields inside the conductor with nonvanishing gradient. In the general case, when the gradient of the solution may vanish, we expect, accordingly to Theorems 1.1, 1.2, that the upper bounds deteriorate as the frequency $F[\varphi]$ given by (1.8) increases. Since $F[\varphi]$ is a ratio which measures the frequency of oscillation of φ , we are interested to investigate on the effectiveness of size estimates approach for oscillating Neumann data.

In particular, the numerical simulations have been carried out for the cubic electrical conductor considered before and choosing the following Neumann data:

$$\left. \begin{aligned} \varphi &= -\cos \frac{n\pi x}{l} && \text{on } z = 0, \\ \varphi &= \cos \frac{n\pi x}{l} && \text{on } z = l, \\ \varphi &= 0 && \text{elsewhere on } \partial\Omega, \end{aligned} \right\} \quad \text{for } n = 0, 1, 2. \quad (2.13)$$

Case $n = 0$ has been already discussed at the beginning of this paragraph and corresponds to the simple case in which the gradient of the unperturbed solution u_0 does not vanish in Ω .

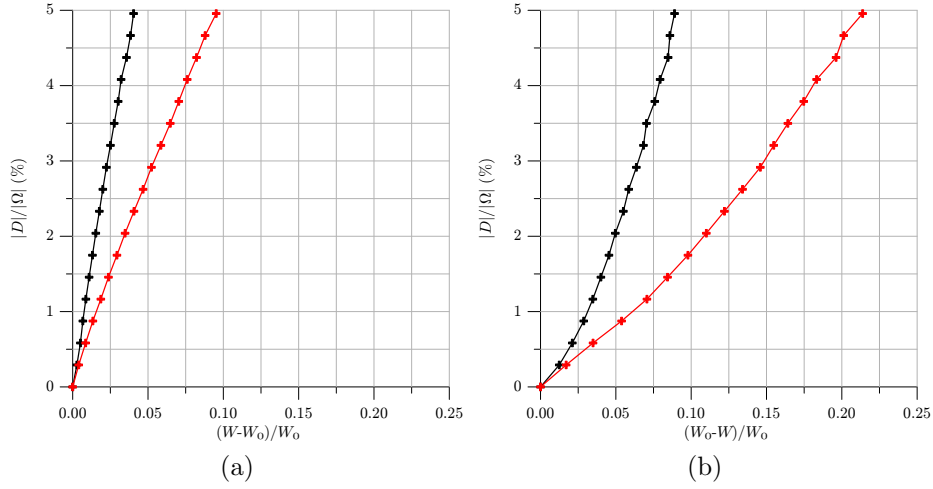


FIGURE 12. Numerical size estimates for inclusions of general shape generated from a generic element belonging to an eight of the cube for test T_2 of Figure 8(a) ($7 \times 7 \times 7$ FE mesh, $d_0 = 1$): $k = 0.1$ (a), $k = 10$ (b).

The two other cases are examples of Neumann data with higher frequency $F[\varphi]$. More precisely, the corresponding solutions u_0 have critical lines of equation

$$\left\{ x = \frac{l}{n} \left(\frac{1}{2} + i \right), z = \frac{l}{n} \left(\frac{1}{2} + j \right) \right\}, \quad i, j = 0, \dots, n-1.$$

The mesh employed is made by $20 \times 20 \times 20$ HC finite elements. The analysis has been focussed on cubic inclusions having volume up to 6% of the total volume of the specimen and conductivity $k = 0.1$ and $k = 10$. The numerical results in case $n = 1$ and $n = 2$ are presented in Figures 13 and 14, respectively. The numerical results show that the lower bound in size estimates (1.10), (1.11) improves as d_0 increases, whereas the upper bound of $|D|$ is rather insensitive to the choice of d_0 .

Theoretical estimates for cases $n = 1$ and $n = 2$ of (2.13) are given by

for $k > 1$:

$$\frac{\tanh \frac{n\pi}{2}}{n\pi(k-1)} \frac{W_0 - W}{W_0} \leq \frac{|D|}{|\Omega|} \leq \frac{1}{C_n} \frac{k}{k-1} \frac{\tanh \frac{n\pi}{2}}{n\pi} \frac{W_0 - W}{W_0}; \quad (2.14)$$

for $k < 1$:

$$\frac{k}{n\pi(1-k)} \tanh \frac{n\pi}{2} \frac{W - W_0}{W_0} \leq \frac{|D|}{|\Omega|} \leq \frac{1}{C_n} \frac{1}{1-k} \frac{\tanh \frac{n\pi}{2}}{n\pi} \frac{W - W_0}{W_0},$$

where

$$C_n = \frac{10}{n\pi \cosh^2 \frac{n\pi}{2}} \left(\sinh \frac{n\pi}{20} - \sin \frac{n\pi}{20} \right), \quad n = 1, 2.$$

The theoretical estimates are indicated in Figures 13 and 14. The slope of the straight line corresponding to the upper bound is so high that it practically coincides with the vertical axis, at least for the portion of graph near the origin considered in this study. The theoretical lower bound gives, for a fixed power gap, values significantly less than those obtained in the numerical experiments.

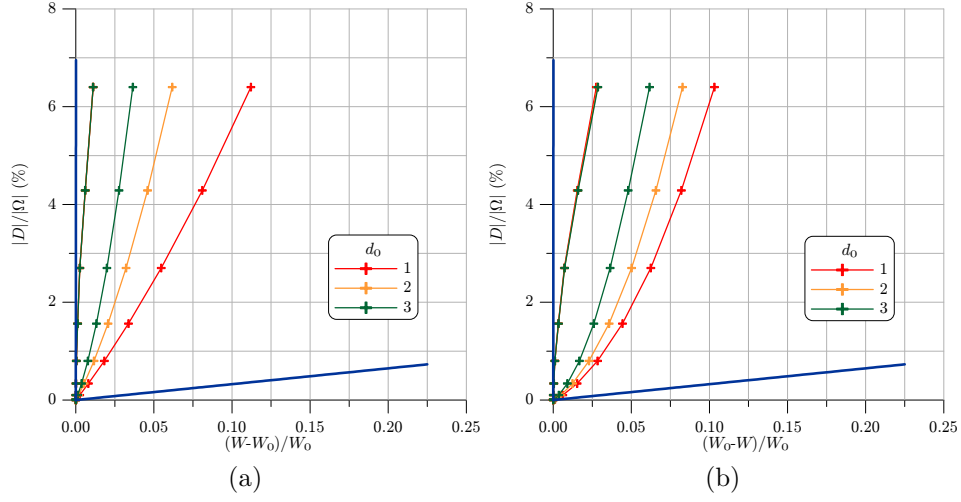


FIGURE 13. Cubic electrical conductor with Neumann data as in case $n = 1$ of (2.13): lower and upper bound of the power gap for different values of d_0 ($k = 0.1$ (a) and $k = 10$ (b)) on a $20 \times 20 \times 20$ mesh.

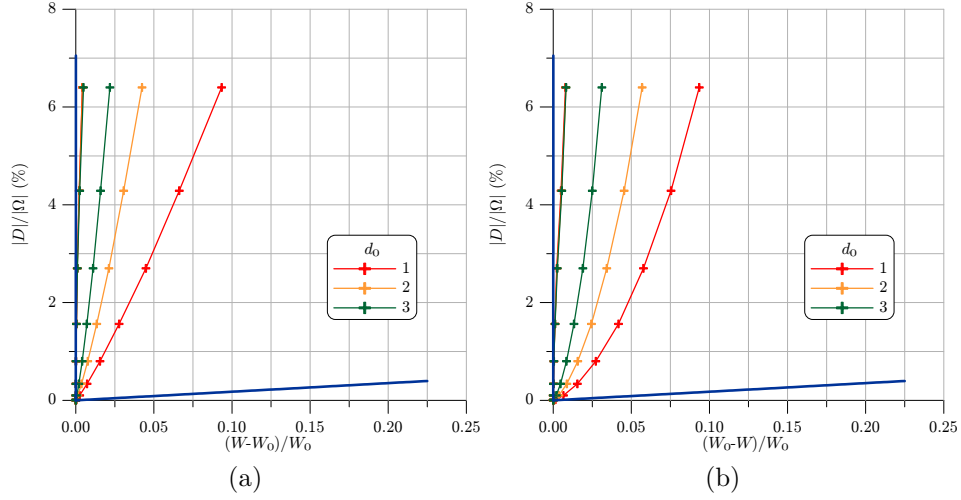


FIGURE 14. Cubic electrical conductor with Neumann data as in case $n = 2$ of (2.13): lower and upper bound of the power gap for different values of d_0 ($k = 0.1$ (a) and $k = 10$ (b)) on a $20 \times 20 \times 20$ mesh.

3. NUMERICAL SIMULATIONS FOR THE COMPLETE EIT MODEL

3.1. Numerical model. In this case, by using the same notation introduced in Section 2, the energy functional $J : H^1(\Omega) \times \mathbb{R}^L \rightarrow \mathbb{R}$ related to the variational

formulation of problem (1.13) is given by

$$J(u, U^l) = \frac{1}{2} \int_{\Omega} (1 + (k-1)\chi_D) \nabla u \cdot \nabla u + \frac{1}{2} \sum_{l=1}^L \frac{1}{z_l} \int_{\partial\Omega_l} (u - U^l)^2 - \sum_{l=1}^L I_l U^l. \quad (3.1)$$

Using HC interpolation for the potential field u and with the notation introduced in Section 2, the discrete energy functional becomes

$$\begin{aligned} J(\mathbf{w}_e, U^l) &= \frac{1}{2} \sum_e \int_{\Omega_e} (1 + (k-1)\chi_D) (\nabla \mathbf{N}_e \mathbf{w}_e) \cdot (\nabla \mathbf{N}_e \mathbf{w}_e) + \\ &\quad + \frac{1}{2} \sum_{l=1}^L \frac{1}{z_l} \sum_{\hat{e}} \int_{(\partial\Omega_l)_e} (\mathbf{N}_e \mathbf{w}_e - U^l)^2 - \sum_{l=1}^L I_l U^l, \end{aligned} \quad (3.2)$$

or

$$\begin{aligned} J(\mathbf{w}_e, U^l) &= \frac{1}{2} \sum_e \mathbf{w}_e^T \mathbf{K}_e \mathbf{w}_e + \\ &\quad + \frac{1}{2} \sum_{l=1}^L \frac{1}{z_l} \sum_{\hat{e}} (\mathbf{w}_e^T \mathbf{K}_{ll} \mathbf{w}_e + (U^l)^2 - 2 \mathbf{w}_e^T \mathbf{K}_{el} U^l) - \sum_{l=1}^L I_l U^l, \end{aligned} \quad (3.3)$$

having used the compact notation

$$\begin{aligned} \mathbf{K}_e &= \int_{\Omega_e} (1 + (k-1)\chi_D) (\nabla \mathbf{N}_e)^T \nabla \mathbf{N}_e, \\ \mathbf{K}_{ll} &= \int_{(\partial\Omega_l)_e} \mathbf{N}_e^T \mathbf{N}_e, \\ \mathbf{K}_{el} &= \int_{(\partial\Omega_l)_e} \mathbf{N}_e^T. \end{aligned} \quad (3.4)$$

We remark that the second sum in the right hand side of (3.2) and (3.3), that on \hat{e} , is extended only to the elements under the electrodes.

Collecting the unknown parameters representing the potential field in \mathbf{w} , those of the electrodes in \mathbf{U} and the current pattern in \mathbf{I} , by a standard method of assembling we obtain the following linear system

$$\begin{bmatrix} \mathbf{K}_{ww} & -\mathbf{K}_{wU} \\ -\mathbf{K}_{wU}^T & \mathbf{K}_{UU} \end{bmatrix} \begin{bmatrix} \mathbf{w} \\ \mathbf{U} \end{bmatrix} = \begin{bmatrix} \mathbf{0} \\ \mathbf{I} \end{bmatrix}, \quad (3.5)$$

which can be efficiently solved taking advantage of the particular structure of coefficient matrix.

3.2. Results for 3-D cases. The analysis has been restricted to the case of two electrodes located on the boundary of a cubic electrical conductor of side l , see Figure 15. The specimen has been discretized by a mesh of $17 \times 17 \times 17$ cubic HC finite elements and the numerical experiments have been carried out on cubic inclusions only, with volume up to 6% of the total volume and conductivity value $k = 0.1$ or $k = 10$. The surface impedance takes a constant value such that $\zeta = \frac{z\sigma}{l} = 0.2$ on both electrodes, according to properties of human skin reported in literature, see, for instance, [26].

In test T_1 of Figure 15, the electrodes cover completely two opposite faces of the specimen, whereas in Test T_2 one electrode coincides with a face of $\partial\Omega$ and the other is a square, formed by one or nine surface finite elements, and it is located in central position of the opposite face. Finally, in Test T_3 , two electrodes are placed

on the same face of the conductor Ω in a symmetric way respect to middle lines of the face. The electrodes are separated by three finite elements and their dimensions are equal to the element size.

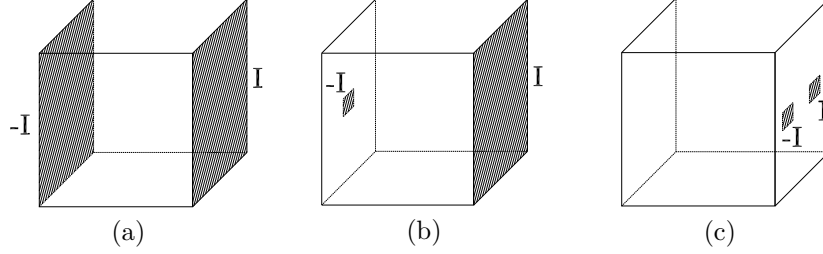


FIGURE 15. Cubic conductor considered in 3-D numerical simulations for the physical EIT model and location of the electrodes: test T_1 (a), test T_2 (b) and test T_3 (c).

The numerical results for Test T_1 are presented in Figure 16 for $k = 0.1$ and $k = 10$, respectively, and for varying values of d_0 . For both cases $k = 0.1$ and $k = 10$, the theoretical size estimates are given by

$$\frac{1}{9} \left(\frac{l+2z}{l} \right) \frac{|W - W_0|}{W_0} \leq \frac{|D|}{|\Omega|} \leq \frac{10}{9} \left(\frac{l+2z}{l} \right) \frac{|W - W_0|}{W_0}$$

and, again, they lead to a rather pessimistic evaluation of the upper and lower bounds.

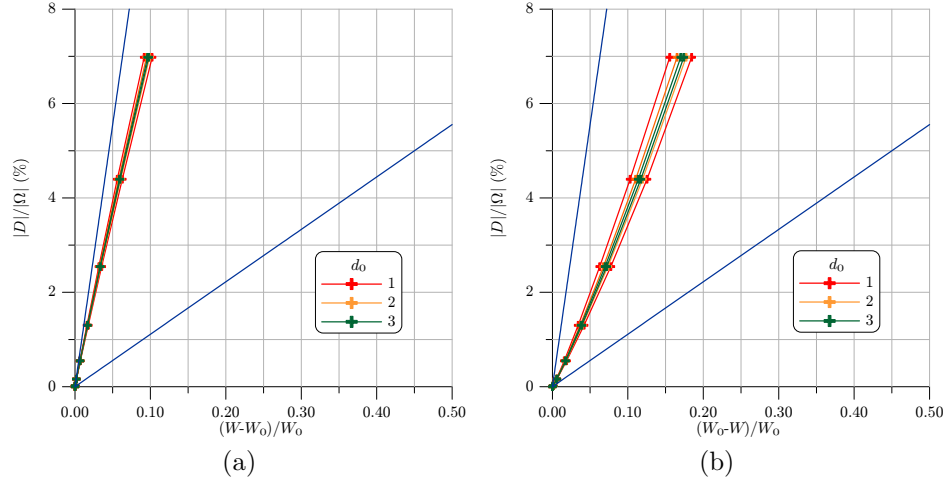


FIGURE 16. Influence of d_0 for cubic inclusions in Test T_1 of Figure 15(a) ($17 \times 17 \times 17$ FE mesh, $\zeta = 0.2$): $k = 0.1$ (a), $k = 10$ (b).

Concerning Test T_2 , Figure 17 shows the results when the small electrode coincides with one surface finite element, whereas Figure 18 refers to the case of a 3×3 finite elements electrode. One can notice that in all the four cases, the upper bound is not really influenced by the value of d_0 . Moreover, the inaccuracy in determining

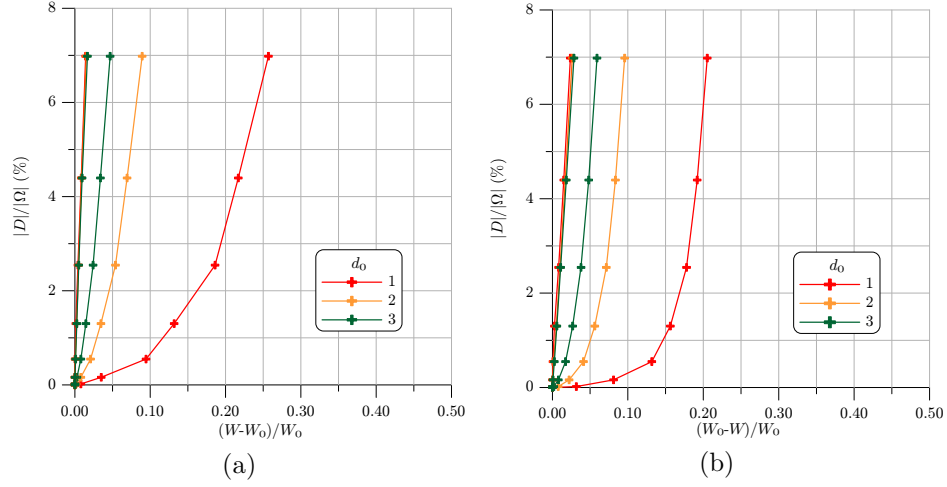


FIGURE 17. Influence of d_0 for cubic inclusions in Test T_2 of Figure 15(b) ($17 \times 17 \times 17$ FE mesh, $\zeta = 0.2$, 1×1 FE electrode): $k = 0.1$ (a), $k = 10$ (b).

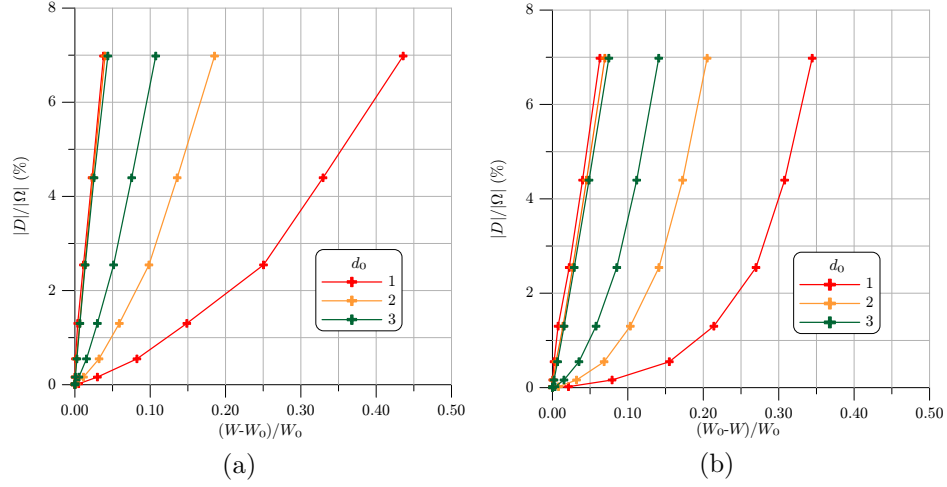


FIGURE 18. Influence of d_0 for cubic inclusions in Test T_2 of Figure 15(b) ($17 \times 17 \times 17$ FE mesh, $\zeta = 0.2$, 3×3 FE electrode): $k = 0.1$ (a), $k = 10$ (b).

the lower bound of the angular sector, is probably due to the fact that the present analysis is restricted to the special class of cubic inclusions.

A comparison between Figure 17 and Figure 18 suggests that better upper bounds can be obtained by enlarging the size of the small electrode. Moreover, from Figures 17 and 18 it appears clearly that the lower bound significantly improves as the distance d_0 between the inclusion D and the boundary of Ω increases. This property has been further investigated by increasing only the distance d_{03} of the inclusion D from the face of the conductor containing the small electrode.

Figure 19 shows the results of simulations in the case of a single finite element electrode and a comparison with Figure 17 suggests that the improvement of the lower bound is mainly due to the greater distance from the electrode.

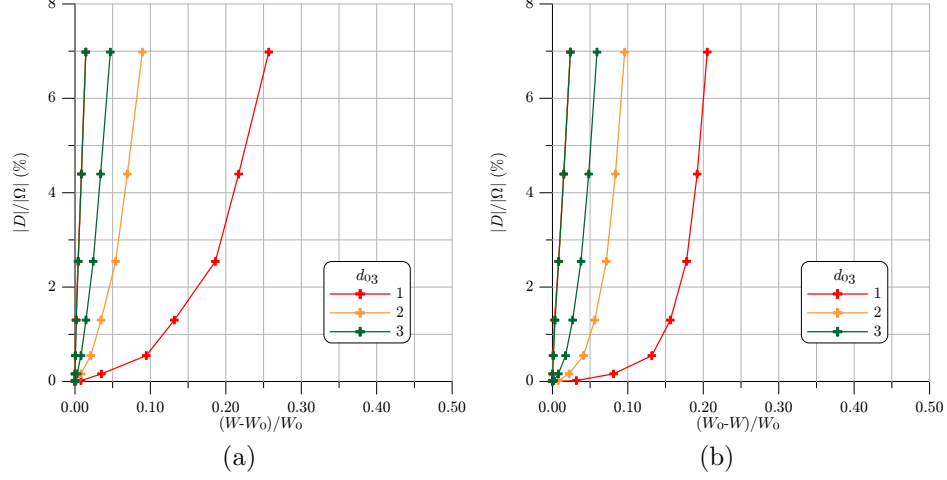


FIGURE 19. Influence of d_{03} for cubic inclusions in Test T_2 of Figure 15(b) ($17 \times 17 \times 17$ FE mesh, $\zeta = 0.2$, 1×1 FE electrode): $k = 0.1$ (a), $k = 10$ (b).

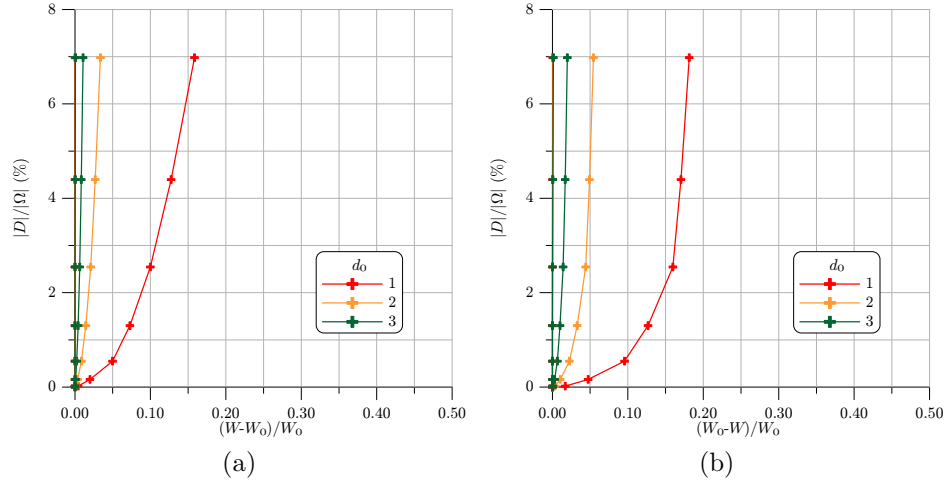


FIGURE 20. Influence of d_0 for cubic inclusions in Test T_3 of Figure 15(c) ($17 \times 17 \times 17$ FE mesh, $\zeta = 0.2$, 1×1 FE electrode): $k = 0.1$ (a), $k = 10$ (b).

Finally, the results of the numerical simulations for Test T_3 are presented in Figure 20. In this case, the lower bound improves as the distance d_0 between the inclusion D and the boundary of Ω increases, whereas the upper bound is indistinguishable from the vertical axis.

4. CONCLUSIONS

We have tested by numerical simulations the approach of *size estimates* for EIT. We could perform experiments in the 2-D setting with a large varieties of shapes of inclusions and we found quite satisfactory bounds, which in some cases are markedly better than those derived theoretically.

In the 3-D case, we had to limit the variety of shapes of the test inclusions since the growth of their degree of freedom conflicts with the limitations on computer time. We showed that good volume bounds hold when the boundary data φ is *well-behaved* in terms of its frequency, whereas they rapidly deteriorate as the frequency increases.

For the complete EIT model we have also made tests in a 3-D setting and compared the bounds in terms of the size of the electrodes, their relative distance and their a-priori assumed distance from the inclusion D . We have shown that we obtain good bounds when the electrodes are not too small and when D is sufficiently away from them.

REFERENCES

- [1] G. ALESSANDRINI, *Stable determination of conductivity by boundary measurements*, Appl. Anal., 27 (1988), pp. 153–172.
- [2] N. MANDACHE, *Exponential instability in an inverse problem for the Schrödinger equation*, Inverse Problems, 17 (2001), pp. 1435–1444.
- [3] G. ALESSANDRINI AND S. VESSELLA, *Lipschitz stability for the inverse conductivity problem*, Adv. Appl. Math, 35 (2005), pp. 207–241.
- [4] A. FRIEDMAN, *Detection of mines by electric measurements*, SIAM J. Appl. Math., 47 (1987), pp. 201–212.
- [5] A. FRIEDMAN AND B. GUSTAFSSON, *Identification of the conductivity coefficient in an elliptic equation*, SIAM J. Math. Anal., 18 (1987), pp. 777–787.
- [6] A. FRIEDMAN AND V. ISAKOV, *On the uniqueness in the inverse conductivity problem with one measurement*, Indiana Univ. Math. J., 38 (1989), pp. 563–579.
- [7] G. ALESSANDRINI AND V. ISAKOV, *Analyticity and uniqueness for the inverse conductivity problem*, Rend. Istit. Mat. Univ. Trieste, 28 (1996), pp. 351–370.
- [8] E. FABES, H. KANG AND J.K. SEO, *Inverse conductivity problem with one measurement: error estimates and approximate identification for perturbed disks*, SIAM J. Math. Anal., 30 (1999), pp. 699–720.
- [9] G. ALESSANDRINI, V. ISAKOV AND J. POWELL, *Local uniqueness in the inverse conductivity problem with one measurement*, Trans. Amer. Math. Soc., 347 (1995), pp. 3031–3041.
- [10] V. ISAKOV, *On uniqueness of recovery of a discontinuous conductivity coefficient*, Comm. Pure Appl. Math., 41 (1988), pp. 865–877.
- [11] V. ISAKOV, *Inverse Problems for Partial Differential Equations*, Springer-Verlag, New York, 1998.
- [12] M. DI CRISTO AND L. RONDI, *Examples of exponential instability for inverse inclusion and scattering problems*, Inverse Problems, 19 (2003), pp. 685–701.
- [13] G. ALESSANDRINI AND E. ROSSET, *The inverse conductivity problem with one measurement: bounds on the size of the unknown object*, SIAM J. Appl. Math., 58 (1998), pp. 1060–1071.
- [14] H. KANG, J.K. SEO AND D. SHEEN, *The inverse conductivity problem with one measurement: stability and estimation of size*, SIAM J. Math. Anal., 28 (1997), pp. 1389–1405.
- [15] G. ALESSANDRINI, E. ROSSET AND J. K. SEO, *Optimal size estimates for the inverse conductivity problem with one measurement*, Proc. Amer. Math. Soc., 128 (2000), pp. 53–64.
- [16] G. ALESSANDRINI, A. MORASSI AND E. ROSSET, *Size estimates*, in Inverse Problems: Theory and Applications, G. Alessandrini and G. Uhlmann, eds., Contemp. Math. 333, AMS, Providence, RI, 2003, pp. 1–33.
- [17] M. IKEHATA, *Size estimation of inclusion*, J. Inverse Ill-Posed Probl., 6 (1998), pp. 127–140.

- [18] G. ALESSANDRINI, A. MORASSI AND E. ROSSET, *Detecting an inclusion in an elastic body by boundary measurements*, SIAM Rev., 46 (2004), pp. 477–498 (revised and updated version of SIAM J. Math. Anal., 3 (2002), pp. 1247–1268).
- [19] G. ALESSANDRINI, A. BILOTTA, G. FORMICA, A. MORASSI, E. ROSSET AND E. TURCO, *Numerical size estimates of inclusions in elastic bodies*, Inverse Problems, 21 (2005), pp. 133–151.
- [20] K.S. CHENG, D. ISAACSON, J.C. NEWELL AND D.G. GISSER, *Electrode models for electric current computed tomography*, IEEE Trans. Biomed. Eng., 36 (1989), pp. 918–924.
- [21] K. PAULSON, W. BRECKON AND M. PIDCOCK, *Electrode modelling in electrical impedance tomography*, SIAM J. Appl. Math., 52 (1992), pp. 1012–1022.
- [22] E. SOMERSALO, M. CHENEY AND D. ISAACSON, *Existence and uniqueness for the electrode models for electric current computed tomography*, SIAM J. Appl. Math., 52 (1992), pp. 1023–1040.
- [23] G. ALESSANDRINI AND E. ROSSET, *Volume bounds of inclusions from physical EIT measurements*, Inverse Problems, 20 (2004), pp. 575–588.
- [24] M. ARISTODEMO, *A high-continuity finite element model for two-dimensional elastic problems*, Comp. Str., 21 (1985), pp. 987–993.
- [25] A. BILOTTA, G. FORMICA AND E. TURCO *Performances of a high-continuity finite element in three-dimensional elasticity*, Report LabMeC n. 26, www.labmec.unical.it, (2003), submitted to Computer and Structures.
- [26] A. J. SUROWIEC, S.S. STUCHLY, J.R. BARR AND A. SWARUP, *Dielectric properties of breast carcinoma and the surrounding tissues*, IEEE Trans. Biomed. Eng., 35 (1988), pp. 257–263.

^Δ DIPARTIMENTO DI MATEMATICA E INFORMATICA, UNIVERSITÀ DEGLI STUDI DI TRIESTE, TRIESTE, ITALY.

[◦] DIPARTIMENTO DI STRUTTURE, UNIVERSITÀ DELLA CALABRIA, RENDE (CS), ITALY.

[∇] DIPARTIMENTO DI GEORISORSE E TERRITORIO, UNIVERSITÀ DEGLI STUDI DI UDINE, UDINE, ITALY.

^{*} DIPARTIMENTO DI ARCHITETTURA E PIANIFICAZIONE, UNIVERSITÀ DEGLI STUDI DI SASSARI, ALGHERO, ITALY.